bioRxiv preprint doi: https://doi.org/10.1101/018945; this version posted November 11, 2015. The copyright holder for this preprint (which was not certified by peer review) is the author/funder, who has granted bioRxiv a license to display the preprint in perpetuity. It is made available under aCC-BY-NC-ND 4.0 International license.

Surface-driven registration method for the structure-informed segmentation of diffusion MR images☆

Oscar Esteban[a,b,*], Dominique Zosso[c], Alessandro Daducci[d], Meritxell Bach-Cuadra[e,d], María-J. Ledesma-Carbayo[a,b], Jean-Philippe Thiran[d,e], Andres Santos[a,b]

[a]*Biomedical Image Technologies (BIT), ETSI Telecomunicación, Universidad Politécnica de Madrid, Madrid, Spain*
[b]*Centro de Investigación Biomédica en Red en Bioingeniería, Biomateriales y Nanomedicina (CIBER-BBN), Spain*
[c]*Department of Mathematics, University of California, Los Angeles (UCLA), Los Angeles, CA, US*
[d]*Signal Processing Laboratory (LTS5), École Polytechnique Fédérale de Lausanne (EPFL), Lausanne, Switzerland*
[e]*Dept. of Radiology, CIBM, University Hospital Center (CHUV) and University of Lausanne (UNIL), Lausanne, Switzerland*

Abstract

Current methods for processing diffusion MRI (dMRI) to map the connectivity of the human brain require precise delineations of anatomical structures. This requirement has been approached either segmenting the data in native dMRI space or mapping the structural information from T1-weighted (T1w) images. The characteristic features of diffusion data in terms of signal-to-noise ratio, resolution, as well as the geometrical distortions caused by the inhomogeneity of magnetic susceptibility across tissues hinder both solutions. Unifying the two approaches, we propose *regseg*, a surface-to-volume nonlinear registration method that segments homogeneous regions within multivariate images by mapping a set of nested reference-surfaces. Accurate surfaces are extracted from a T1w image of the subject, using as target image the bivariate volume comprehending the fractional anisotropy (FA) and the apparent diffusion coefficient (ADC) maps derived from the dMRI dataset. We first verify the accuracy of *regseg* on a general context using digital phantoms. Then we establish an evaluation framework using undistorted dMRI data from the Human Connectome Project (HCP) and known deformations derived from real inhomogeneity fieldmaps. We analyze the performance of *regseg* computing the misregistration error of the surfaces estimated after being mapped with *regseg* onto 16 datasets from the HCP. The distribution of errors shows a 95% CI of 0.56–0.66 mm, that is below the dMRI resolution (1.25 mm, isotropic). Finally, we cross-compare the proposed tool against a nonlinear *b0*-to-T2w registration method, thereby obtaining a significantly lower misregistration error with *regseg*. Therefore, we demonstrate that *regseg* allows the accurate mapping of structural information in dMRI space, enabling the application of new structure-informed techniques in the connectome extraction.

Keywords: active surfaces, cortical parcellation, diffusion MRI, nonlinear registration, segmentation, susceptibility distortion.

1. Introduction

Diffusion MRI enables the mapping of microstructure (Basser and Pierpaoli, 1996) and connectivity (Craddock et al., 2013) of the human brain *in-vivo*. It is generally acquired using echo-planar imaging (EPI) schemes, since they are very fast at scanning a large sequence of images called diffusion weighted images (DWIs). Each DWI is sensitized with a gradient to probe proton diffusion in a certain orientation. Subsequent processing involves describing the local microstructure with one of the available models, which range

☆Supplemental materials to this work have been submitted to Data in Brief (Esteban et al., 2015). During the review process, the document is available in doi:10.6084/m9.figshare.1397502.

*Corresponding author
Email address: phd@oscaresteban.es (Oscar Esteban)

bioRxiv preprint doi: https://doi.org/10.1101/018945; this version posted November 11, 2015. The copyright holder for this preprint (which was not certified by peer review) is the author/funder, who has granted bioRxiv a license to display the preprint in perpetuity. It is made available under aCC-BY-NC-ND 4.0 International license.

from the early diffusion tensor imaging (DTI) proposed by Basser and Pierpaoli (1996) to current models such as (Daducci et al., 2015). The microstructural map is then used to draw the preferential orientations of diffusion across the brain using tractography (Mori et al., 1999). Finally, a graph representing the corresponding structural network is built using the regions of a cortical parcellation as nodes and the fiber paths found by tractography as edges (Hagmann et al., 2008). The methodologies to solve reconstruction, tractography and network building require the delineation of the anatomy in the dMRI space. Moreover, current trends on reconstruction (Jeurissen et al., 2014) and tractography (Smith et al., 2012) are increasingly using structural information to improve the microstructural mapping and fiber-tracking.

Possibly, the earliest structural information incorporated to aid dMRI processing is the white matter (WM) mask used as a termination criteria for tractography. The standardized procedure to obtain this mask was thresholding the FA map. However, the mask and subsequent analyses are highly dependent on the threshold set (Taoka et al., 2009). To overcome the unreliability of FA thresholding, and to broaden WM segmentation to brain tissue segmentation, a large number of methods have been proposed using DWIs, the *b0*, and DTI-derived scalar maps such as FA, ADC and others (Zhukov et al., 2003; Rousson et al., 2004; Jonasson, 2005; Hadjiprocopis et al., 2005; Liu et al., 2007; Lu et al., 2008; Han et al., 2009). However, the precise segmentation of dMRI is difficult for several reasons. First, dMRI images have a resolution that is much lower than that of the imaged microstructural features. Therefore, voxels located in structural discontinuities are affected by partial voluming of the signal sources. Second, the extremely low signal-to-noise ratio (SNR) and the high dimensionality of the DWIs prevent their direct use in segmentation. Third, the low contrast between grey matter (GM) and WM in the *b0* volume also makes it unsuitable for brain tissue segmentation.

An alternative route to segmentation in dMRI space is the mapping of the structural information extracted from anatomical MR images, such as T1w, using image registration techniques. Generally, intra-subject registration of MR images of the brain involves only a linear mapping to compensate for head motion between scans. However, EPI introduces a geometrical distortion (Jezzard and Balaban, 1995) that impedes the linear mapping from the structural space. Numerous methods have been proposed to overcome this problem by incorporating information from extra MR acquisitions such as fieldmaps (Jezzard and Balaban, 1995), DWIs with a different phase-encoding (PE) scheme (Cordes et al., 2000; Chiou and Nalcioglu, 2000), or T2-weighted (T2w) images (Kybic et al., 2000; Studholme et al., 2000). These methods estimate the deformation field associated to *EPI distortions* and resample the DWIs onto a corrected dMRI space. The retrospective EPI correction is an active field of research yielding frequent refinements and combinations of the original methods, such as (Holland et al., 2010; Andersson et al., 2012; Irfanoglu et al., 2015). A standardized method to solve the remaining linear mapping between the corrected-dMRI and the structural spaces is *bbregister* (Greve and Fischl, 2009).

Here, we present a segmentation and surface-to-volume registration method named *regseg*, and show its usefulness in mapping anatomical information from structural space into native dMRI space to aid subsequent processing steps (reconstruction, tractography and network building using a cortical parcellation). The underlying hypothesis is that the registration and segmentation problems in dMRI can be solved simultaneously. To implement *regseg* we first establish an active contours without edges (Chan and Vese, 2001) segmentation framework. A specific set of reference surfaces extracted from the same subject initialize the 3D active contours, which evolve searching for homogeneous regions in the multivariate target-image. In the presented application to segment dMRI data, we propose to use *regseg* using a set of nested surfaces extracted from a structural image (e.g. T1w) and a bivariate target-volume comprehending the FA and ADC maps as inputs. The evolution of the surfaces is supported by a B-spline basis, optimized iteratively using a descent approach driven by shape-gradients (Jehan-Besson et al., 2003; Herbulot et al., 2006). Therefore, *regseg* establishes a registration framework that actually deals with the nonlinear warping induced by EPI distortions. *Regseg* integrates the benefits of segmentation and registration methods together and exploits the multivariate nature of dMRI data to contribute in the proposed application on three key aspects: 1) it avoids the resampling the DWIs introduced by the correction of EPI distortions, since processing can be performed on the native dMRI space; 2) the surfaces are typically extracted from the T1w image of the same subject, therefore *regseg* does not require additional MR acquisitions to the minimal dMRI protocol; and 3) *regseg* increases the geometrical accuracy of the overall process. In this paper, we first verify the

bioRxiv preprint doi: https://doi.org/10.1101/018945; this version posted November 11, 2015. The copyright holder for this preprint (which was not certified by peer review) is the author/funder, who has granted bioRxiv a license to display the preprint in perpetuity. It is made available under aCC-BY-NC-ND 4.0 International license.

functionality of the method and the *regseg* implementation using a set of digital phantoms, demonstrating the sub-pixel accuracy in registration. We then evaluate *regseg* on real dMRI datasets, using a derivation of our instrumentation framework (Esteban et al., 2014a) which simulates known and realistic EPI distortions. We also compare *regseg* and a nonlinear registration method to map the *b0* to the corresponding T2w image of the same subject. This method is a derivation of the T2w-registration based (T2B) correction methods (Kybic et al., 2000), reproducing the settings of an existing implementation included within a widely used diffusion processing software (*ExploreDTI*, Leemans et al., 2009). With this comparison, we demonstrate how *regseg* achieves higher accuracy with the simultaneous registration and segmentation process.

2. Methods

2.1. Registration framework and segmentation model

Let $\mathbf{\Gamma}_R = \{\Gamma_m : m \in \mathbb{N}, m \leq N_S\}$ be the set of N_S surfaces extracted from the undistorted T1w image (the reference space R). We reformulate the segmentation of the distorted dMRI images (the moving space M) as a registration problem where we search for an underlying deformation field U such that the structures in R defined by $\mathbf{\Gamma}_R$ align optimally with their corresponding structures in M:

$$\begin{aligned} U\colon R \subset \mathbb{R}^n &\to M \subset \mathbb{R}^n \\ \mathbf{r} &\mapsto \mathbf{r}' = \mathbf{r} + \mathbf{u}(\mathbf{r}), \end{aligned} \tag{1}$$

where $\mathbf{r}$ denotes a position in R, $\mathbf{r}'$ is its corresponding location in M, and n denotes the dimensionality of images. Finally, $\mathbf{u} = \mathbf{u}(\mathbf{r})$ is the displacement of every point with respect to the reference domain. The general overview of how the surfaces interact with the registration framework is presented in Figure 1.

Cost-function derivation. In a Bayesian framework for registration (Wyatt and Noble, 2003; Pohl et al., 2006; Gass et al., 2014), the mappings U in (1) are evaluated based on their posterior probability given the observed data M. Let $\mathbf{\Omega} = \{\Omega_l : l \in \mathbb{N}, l \leq N_L\}$ be the set of N_L competing regions in which M is partitioned by the projection of $\mathbf{\Gamma}_R$. Using Bayes' rule, the posterior likelihood is computed as:

$$P(U \mid M, \mathbf{\Omega}) = \frac{P(M \mid U, \mathbf{\Omega})\, P(U)}{P(M)}, \tag{2}$$

where $P(M \mid U, \mathbf{\Omega})$ is the data likelihood. Since $\mathbf{\Omega}$ are mapped by U, we simplify $P(U, \mathbf{\Omega}) = P(U) \implies P(M \mid U, \mathbf{\Omega}) = P(M \mid U)$. The best estimate $\hat{U}$ then satisfies the maximum a posteriori criterion and it aligns $\mathbf{\Gamma}_R$ into M. First, we assume independence between pixels, and thus we break down the global data likelihood into a product of pixel-wise conditional probabilities:

$$P(M \mid U) = \prod_l \prod_{\mathbf{r} \in \Omega_l} P\left(\mathbf{f}' \mid U\right), \tag{3}$$

where $\mathbf{f}' = M(\mathbf{r}')$ is the feature vector at the displaced position $\mathbf{r}'$ (1) in the moving image. For convenience and because it has been shown to be an appropriate approximation (Van Leemput et al., 1999; Cuadra et al., 2005), we introduce two assumptions for each region Ω_l: 1) the features are i.i.d.; and 2) they can be modeled by multivariate normal distributions (Esteban et al., 2014b) with parameters $\{\boldsymbol{\mu}_l, \mathbf{\Sigma}_l\}$ for each region Ω_l. Even though the features being segmented are not generally i.i.d., the spatial interdependency of voxels is implicitly supported by the piecewise smooth partition of the space $\mathbf{\Omega}$. In Figure 2 it is shown that marginal distributions of data can be approximated by multivariate normal distributions. Therefore,

bioRxiv preprint doi: https://doi.org/10.1101/018945; this version posted November 11, 2015. The copyright holder for this preprint (which was not certified by peer review) is the author/funder, who has granted bioRxiv a license to display the preprint in perpetuity. It is made available under aCC-BY-NC-ND 4.0 International license.

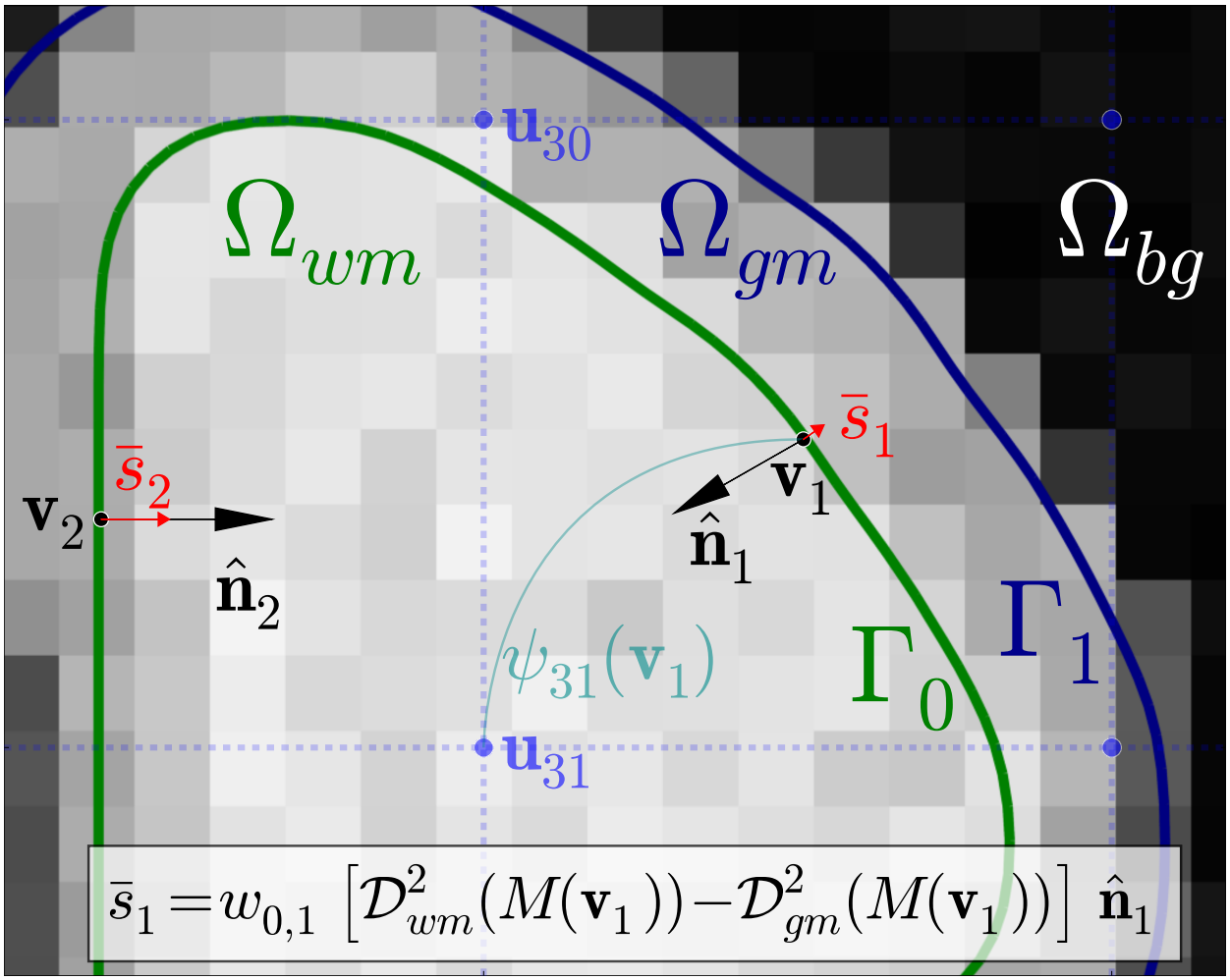

Figure 1: The active contours are defined as the interfacing surfaces of the competing ROIs Ω_l, which are represented in green and dark blue in this close-up. They evolve iteratively following their inward normals $\hat{n}_i$ at each vertex $\mathbf{v}_i$ of the mesh. The gradient speeds $\bar{s}_i$ drive registration, which are computed as the disparity of the data energies with respect to the two limiting regions of $M(\mathbf{v}_i)$, the features of the image M in the location of vertex $\mathbf{v}_i$ (see Supplemental Materials, equation SM5). In this figure, $\bar{s}_1$ is written in the lower box, with Ω_{wm} in the inner limiting region, Ω_{gm} the outer region, and $w_{0,1}$ is the relative area associated with vertex $\mathbf{v}_1$ with respect to the total area of surface Γ_0.

bioRxiv preprint doi: https://doi.org/10.1101/018945; this version posted November 11, 2015. The copyright holder for this preprint (which was not certified by peer review) is the author/funder, who has granted bioRxiv a license to display the preprint in perpetuity. It is made available under aCC-BY-NC-ND 4.0 International license.

$$P(M \mid U) = \prod_{l} \prod_{\mathbf{r}\in\Omega_l} \mathcal{N}(\mathbf{f} \mid \boldsymbol{\mu}_l, \boldsymbol{\Sigma}_l) = \\ = \prod_{l} \prod_{\mathbf{r}\in\Omega_l} \frac{1}{\sqrt{(2\pi)^C \ |\boldsymbol{\Sigma}_l|}} e^{\left(-\frac{1}{2}\mathcal{D}_l^2(\mathbf{f}')\right)}, \tag{4}$$

using $\mathcal{D}_l^2(\mathbf{f})$ to denote the squared *Mahalanobis distance* of $\mathbf{f}$ with respect to the descriptors of region l as $\mathcal{D}_l^2(\mathbf{f}) = (\mathbf{f} - \boldsymbol{\mu}_l)^T \boldsymbol{\Sigma}_l{}^{-1} (\mathbf{f} - \boldsymbol{\mu}_l)$. C is the number of channels comprised in the image M. In fact, the projection of $\boldsymbol{\Gamma}_R$ onto M is an implicit segmentation model, for which the covariance matrix $\boldsymbol{\Sigma}_l$ of each region is minimized. In Figure 2, this minimization is illustrated for the segmentation of the FA and the ADC maps of one subject.

Regularization. The smoothness of the resulting displacements field is induced by a Thikonov regularization prior:

$$P(U) = \prod_{\mathbf{r}} p(\mathbf{u}) = \prod_{\mathbf{r}} p_0(\mathbf{u})\, p_1(\mathbf{u}), \text{ with} \tag{5}$$

$$p_0(\mathbf{u}) = \mathcal{N}(\mathbf{u} \mid 0, \mathbf{A}^{-1}), \\ p_1(\mathbf{u}) = \mathcal{N}(\nabla\mathbf{u} \mid 0, \mathbf{B}^{-1}), \tag{6}$$

which requires that the distortion and its gradient have zero mean and variance governed by the matrices $\mathbf{A}$ and $\mathbf{B}$. Finally, the maximum a posteriori problem is adapted to a variational problem where we search for the minimum of an energy functional by applying $E(\mathbf{u}) = -\log\{P(M \mid U)\, P(U)\}$:

$$E(\mathbf{u}) = -\log \prod_{l} \prod_{\mathbf{r}\in\Omega_l} \mathcal{N}\left(\mathbf{f}' \mid \boldsymbol{\mu}_l, \boldsymbol{\Sigma}_l\right)\, p_0(\mathbf{u})\, p_1(\mathbf{u}) = \\ = \text{Const.} + \sum_{l} \int_{\Omega_l} \mathcal{D}_l^2(\mathbf{f}')\, d\mathbf{r} + \\ + \int_{\Omega} \frac{1}{2} \left[\mathbf{u}^T \mathbf{A} \mathbf{u} + (\nabla\mathbf{u})^T \mathbf{B} (\nabla\mathbf{u})\right]\, d\mathbf{r}. \tag{7}$$

This expression is the dual of the Mumford-Shah functional that corresponds to the framework of active contours without edges (Chan and Vese, 2001) with the anisotropic regularization term of Nagel and Enkelmann (1986).

2.2. Numerical Implementation

Deformation model. Since the vertices of the surfaces $\{\mathbf{v}_i : \mathbf{v}_i \subset \boldsymbol{\Gamma}\}_{i=1\ldots N_V}$ are probably located off-grid, it is necessary to derive $\mathbf{u}_i = \mathbf{u}(\mathbf{v}_i)$ from a discrete set of parameters $\{\mathbf{u}_k\}_{k=1\ldots K}$. Densification is achieved using a set of associated basis functions ψ_k (8). In our implementation, ψ_k is a tensor-product B-spline kernel of degree three.

$$\mathbf{v}_i' = \mathbf{v}_i + \mathbf{u}_i = \mathbf{v}_i + \sum_{k} \psi_k(\mathbf{r})\, \mathbf{u}_k. \tag{8}$$

bioRxiv preprint doi: https://doi.org/10.1101/018945; this version posted November 11, 2015. The copyright holder for this preprint (which was not certified by peer review) is the author/funder, who has granted bioRxiv a license to display the preprint in perpetuity. It is made available under aCC-BY-NC-ND 4.0 International license.

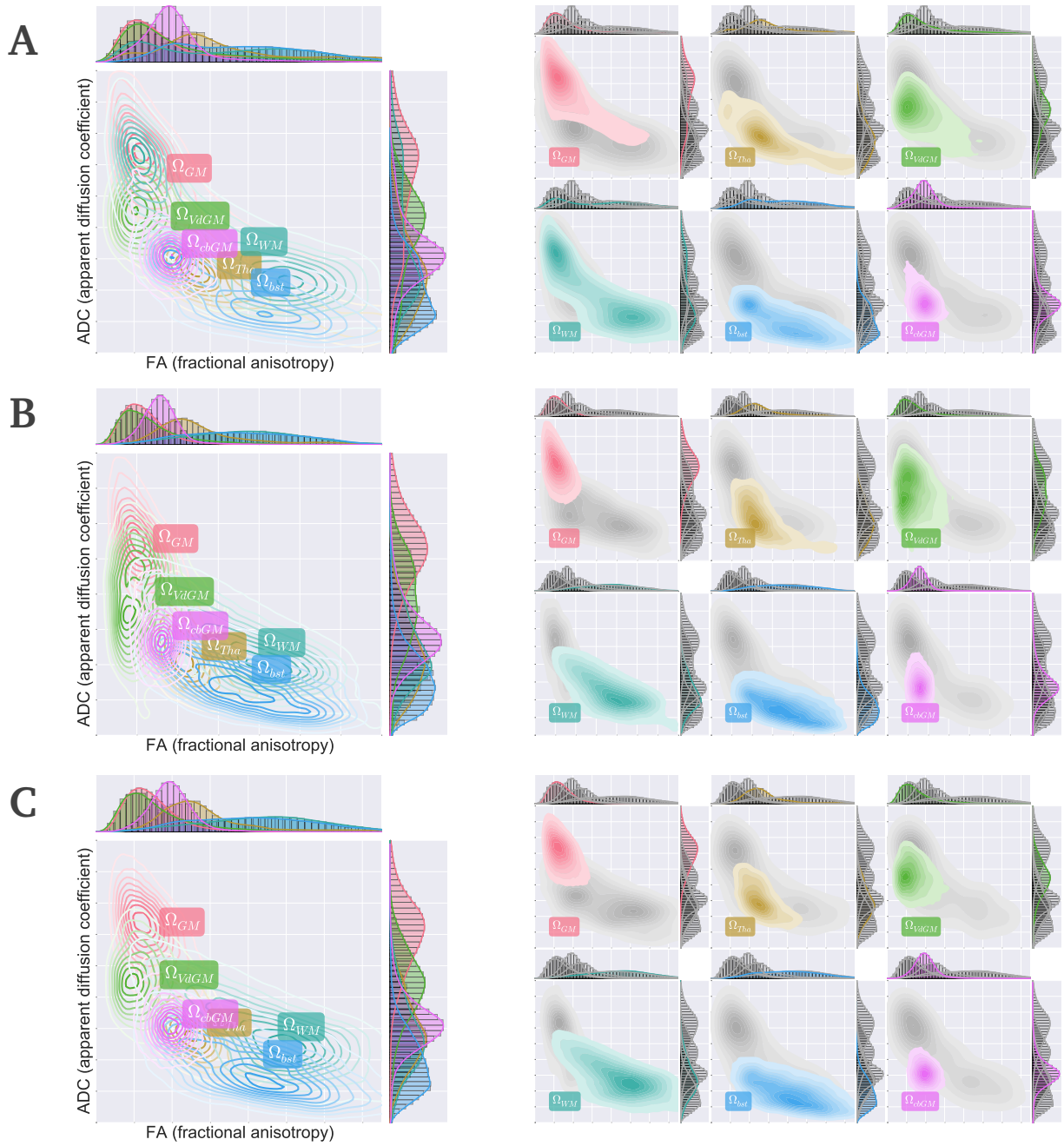

Figure 2: Evolution of the segmentation model defined by the homogeneous regions Ω_l for a real dataset. The left plot in each panel represents a kernel density estimate of the location and spread of each region Ω_l in the bivariate feature space of M, which comprises the FA and ADC maps. At the top and the right margins, the marginal distributions of Ω_l on the FA and ADC are respectively displayed. On the right side, the sampled distribution of each region is shown in small scatter plot, in contrast to the complete bivariate data. A) shows the initialization of the model, when the anatomically-correct surfaces are not mapped into the dMRI space. The panel shows the resulting conditional distributions of segmenting the (distorted) FA and ADC maps with the original (undistorted) surfaces. Panel B shows the equivalent information, using the surfaces that are perfectly mapped into the distorted dMRI space. Since the surfaces are now aligned in M, the spreads of the conditional distributions for each region are reduced with respect to those in A. Panel C, after *regseg* registration, shows how the covariance matrices $\mathbf{\Sigma}_l$ are minimized with respect to panel A, and the resulting segmentation is close to the theoretical situation presented in panel B.

bioRxiv preprint doi: https://doi.org/10.1101/018945; this version posted November 11, 2015. The copyright holder for this preprint (which was not certified by peer review) is the author/funder, who has granted bioRxiv a license to display the preprint in perpetuity. It is made available under aCC-BY-NC-ND 4.0 International license.

Optimization. To find the minimum of the energy functional (7), we propose a gradient-descent approach with respect to the underlying deformation field using the following partial differential equation (PDE):

$$\frac{\partial \mathbf{u}(\mathbf{r},t)}{\partial t} \propto -\frac{\partial E(\mathbf{u})}{\partial \mathbf{u}_k}, \tag{9}$$

where t is an artificial time parameter of the contour evolution and $\mathbf{u}_k$ are the parameters that support the estimate $\hat{U}$ of the transformation at the current time point. Let us assume that the anisotropy is aligned with the imaging axes to simplify (7) as expression (A.1) in Appendix 1, and thus to compute its derivative (9):

$$\begin{aligned}\frac{\partial E(\mathbf{u})}{\partial \mathbf{u}_k} = \frac{\partial}{\partial \mathbf{u}_k}\Big\{\sum_l \int_{\Omega_l} \mathcal{D}_l^2(\mathbf{f}')\,d\mathbf{r} + \\ + \int_\Omega \frac{1}{2}[\boldsymbol{\alpha}\cdot\mathbf{u}^{\circ 2} + \boldsymbol{\beta}\cdot(\nabla\mathbf{u})^{\circ 2}]\,d\mathbf{r}\Big\},\end{aligned} \tag{10}$$

where $\mathbf{u}^{\circ 2} = \mathbf{u}^T \cdot \mathbf{u}$. Then, the data and regularization terms are split and discretized to compute their derivatives. The computation of the explicit shape gradients at each $\mathbf{v}_i'$ is illustrated in Figure 1. Then, (10) can be reformulated as (see Supplemental Materials, equations SM6-SM12):

$$\frac{\partial E(\mathbf{u})}{\partial \mathbf{u}_k} = \mathbf{g}_k + \boldsymbol{\alpha}\cdot\mathbf{u}_k - \boldsymbol{\beta}\cdot(\Delta\mathbf{u}_k). \tag{11}$$

Finally, to descend this gradient, we establish a semi-implicit Euler scheme (see Supplemental Materials, section S1.3), with a step size parameter δ, which we solve in the spectral domain as follows:

$$\mathbf{u}_k^{t+1} = \mathcal{F}^{-1}\left\{\frac{\mathcal{F}\{\delta^{-1}\,\mathbf{u}_k^t - \mathbf{g}_k\}}{\mathcal{F}\{(\delta^{-1}+\boldsymbol{\alpha})\,I - \boldsymbol{\beta}\Delta\}}\right\}, \tag{12}$$

where I denotes the identity operator.

Implementation details and convergence. The *regseg* tool includes a multiresolution strategy on the free-form deformation field. Registration pyramids are created by setting the spacing between the control points of the B-spline basis functions for each level of the multiresolution strategy. The implementation details as well as other features (such as the sparse matrix approach to fast interpolation) and the main parameters (such as δ, $\boldsymbol{\alpha}$, $\boldsymbol{\beta}$, the B-spline grid resolutions, and target image smoothing) are discussed in the Supplemental Materials, section S1.

2.3. Evaluation protocol

In order to assess the performance of *regseg*, we defined the following general evaluation protocol: 1) Extract the set of undistorted surfaces $\boldsymbol{\Gamma}_R$; 2) Compute a ground-truth field of displacements U_{true}, which is applied to generate warped images (M) for segmentation; 3) Execute *regseg* with $\boldsymbol{\Gamma}_R$ and use the warped data as inputs; and 4) Perform a visual assessment and compute the error metrics.

A first proof of concept is introduced to demonstrate *regseg* in digital phantoms with simple geometries, using U_{true} without directional restrictions. Then, *regseg* is evaluated in a framework using undistorted dMRI datasets, and U_{true} is derived from the corresponding inhomogeneity fieldmap of the subject. Therefore, the deformation field is nonzero only in the PE axis, and resembles a real EPI distortion. The adaptation of the evaluation protocol to the simulated phantoms and the real data is explained in the following sections.

bioRxiv preprint doi: https://doi.org/10.1101/018945; this version posted November 11, 2015. The copyright holder for this preprint (which was not certified by peer review) is the author/funder, who has granted bioRxiv a license to display the preprint in perpetuity. It is made available under aCC-BY-NC-ND 4.0 International license.

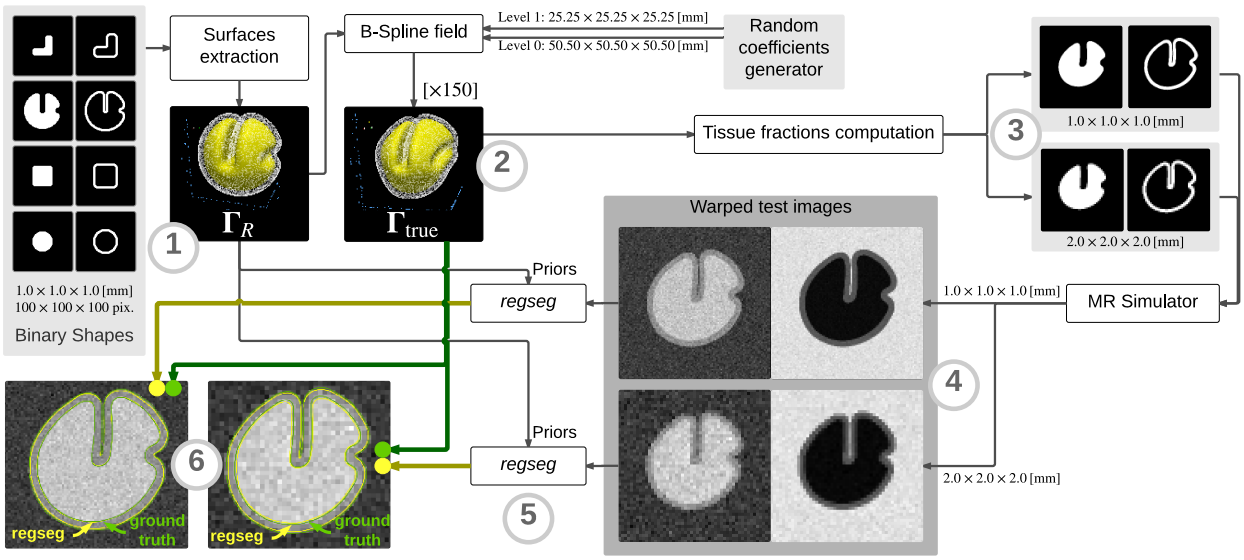

Figure 3: Evaluation of *regseg* using phantom data according to the following instrumental workflow. 1) The reference surfaces $\mathbf{\Gamma}_R$ are triangularized meshes extracted from the four binary shapes (i.e., "box", "ball", "L", "gyrus"). 2) A ground-truth displacement field was generated as described in subsection 2.4, and applied to warp $\mathbf{\Gamma}_R$, thereby obtaining $\mathbf{\Gamma}_{\text{true}}$. 3) After being warped, $\mathbf{\Gamma}_{\text{true}}$ were projected onto the corresponding discrete 3D volume and downsampled to create partial volume effects at two resolutions, i.e., 2.0×2.0×2.0 [mm] and 1.0×1.0×1.0 [mm], thereby producing sets of tissue fractions maps. 4) The tissue fractions were fed into a magnetic resonance (MR) simulator, which generated T1-weighted (T1w) and T2-weighted (T2w) -like images at the two possible resolutions. 5) The *regseg* tool was applied using the warped test images as multispectral moving images and $\mathbf{\Gamma}_R$ as shape priors. 6) The agreement between the surfaces fitted by *regseg* ($\hat{\mathbf{\Gamma}}_{\text{test}}$) and $\mathbf{\Gamma}_{\text{true}}$ were assessed visually using automatically generated visual reports and quantitatively with the Hausdorff distance between the corresponding surfaces.

2.4. *Simulated phantoms*

The workflow required to simulate the digital phantoms and to assess the performance of *regseg* with them is presented in Figure 3. A set of four binary objects (i.e. "box", "ball", "L", and "gyrus") was generated by combining the binarization of analytical shapes and mathematical morphology. The reference surfaces $\mathbf{\Gamma}_R$ were extracted from the binary shapes using *FreeSurfer* tools (Fischl, 2012). The ground-truth distortion was generated using a chain of two displacement fields supported by grids of B-spline basis functions. The coefficients of the basis functions were generated randomly for both levels in their three dimensions. The three components of the displacements $\mathbf{u} = (u_d)$ were bounded above by 40% of the separation between the control points at each level to obtain diffeomorphic transforms after concatenation (Rueckert et al., 2006). The first deformation field was applied to generate large warpings with control points separated by 50.50 mm in the three dimensions ($u_d \leq 20.20$ mm). With the second warping, we aimed to obtain a field with smoothness close to that found in a typical distortion field of dMRI data (Irfanoglu et al., 2011). Therefore, the control points were separated by 25.25 mm ($u_d \leq 10.10$ mm). After generating the ground-truth deformation, the original surfaces were warped by interpolating the displacements field at each vertex. The warped surfaces $\mathbf{\Gamma}_{\text{true}}$ were binarized to generate tissue fractions at low (2.0×2.0×2.0 [mm]) and high (1.0×1.0×1.0 [mm]) resolutions. Using a magnetic resonance (MR) simulator (Caruyer et al., 2014), we synthesized T1w (TE/TR= 10/1500 ms) and T2w images (TE/TR= 90/5000 ms), which corresponded to each phantom type, with each at two resolutions (1.0 mm and 2.0 mm isotropic). The field of view at both resolutions was 100×100×100 [mm]. Next, *regseg* was applied to map $\mathbf{\Gamma}_R$ onto the warped phantoms to obtain the registered surfaces ($\hat{\mathbf{\Gamma}}_{\text{test}}$). To quantify the misregistration error, we computed the Hausdorff distance between $\hat{\mathbf{\Gamma}}_{\text{test}}$ and $\mathbf{\Gamma}_{\text{true}}$ using (Commandeur et al., 2011). In total, 1200 experiments (four phantom types × 150 random warpings × two resolutions) were performed according to the workflow illustrated in Figure 3.

bioRxiv preprint doi: https://doi.org/10.1101/018945; this version posted November 11, 2015. The copyright holder for this preprint (which was not certified by peer review) is the author/funder, who has granted bioRxiv a license to display the preprint in perpetuity. It is made available under aCC-BY-NC-ND 4.0 International license.

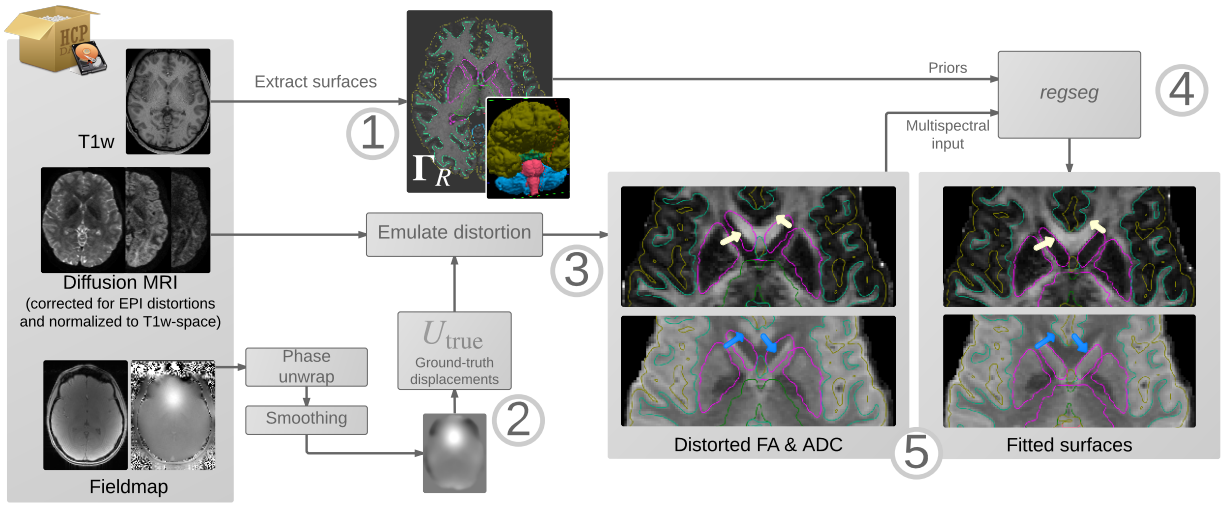

Figure 4: Experimental workflow employed to process real data from the Human Connectome Project (HCP). 1) $\mathbf{\Gamma}_R$ were extracted from the anatomical reference (T1w image). 2) For use as the ground truth, we generated a plausible synthetic distortion U_{true} from the fieldmap with (13). 3) The dMRI data were warped using U_{true} to reproduce the effects of real susceptibility-derived distortions. Target diffusion scalars (FA and ADC) were computed with the distorted data and stacked to feed the multivariate input required by *regseg*. 4) The method was run to obtain $U_{\text{test}} = \hat{U}_{\text{true}}$, i.e., the estimate of the ground-truth deformation. 5) The results were evaluated visually and quantitatively. The arrows point to edges in the target images (light-yellow arrows for FA, blue for ADC) that should be aligned with a surface, showing how distortion limits the direct mapping from the structural space in which the contours are defined.

Segmentation model and settings. The segmentation model of the phantoms is implicitly defined: all phantoms comprehend an inner surface enclosing a uniform WM-like region, and an outer surface wrapping a GM-like layer. The outside is filled with uniform background (see Figure 3). All the experimental settings used for the phantoms are made available in a unique configuration file[1].

2.5. Real datasets

The experimental framework for the real datasets is presented in Figure 4, which extends our previous evaluation (Esteban et al., 2014a) of distortions using dMRI phantoms.

Data. To evaluate *regseg* using real dMRI data obtained from human brains, we collected 16 subjects from the HCP database. The original acquisitions are released within "unprocessed" packages, whereas the "minimally preprocessed" packages contain the corresponding images after some processing (correction for several artifacts, brain-extraction, spatial normalization, etc.). We refer the reader to Van Essen et al. (2012) for exact details of the acquisition parameters and Glasser et al. (2013) for the preprocessing issues. These datasets comprise a large set of images, including T1w, T2w, and multi-shell dMRI images. Since we obtained the dMRI data from the minimally preprocessed package, these images are corrected for EPI distortions and spatially normalized in T1w space.

Segmentation model. Based on our experience and previous studies (Ennis and Kindlmann, 2006), we defined the moving image as a stack of the FA and ADC maps derived from dMRI data. After evaluating several alternative models, we empirically defined a partition $\mathbf{\Omega}$ according to the following six regions: 1) thalamus (Ω_{Tha}); 2) ventricular system and deep GM structures (Ω_{VdGM}); 3) cerebral WM (Ω_{WM}); 4) brain stem and cerebellar WM (Ω_{bst}); 5) cerebellar GM (Ω_{cbGM}); and 6) cortical GM (Ω_{GM}). Using tools in *FreeSurfer* and appropriate selections of labels in the *aparc* segmentation released with the HCP data, we extracted the $\mathbf{\Gamma}_R$ set for the reference surfaces. The segmentation model corresponding to this partition is shown in Figure 2 and discussed in greater detail in the Supplemental Materials, section S4.

[1] `https://github.com/oesteban/RegSeg/blob/master/Scripts/pyacwereg/data/regseg_default.json`

bioRxiv preprint doi: https://doi.org/10.1101/018945; this version posted November 11, 2015. The copyright holder for this preprint (which was not certified by peer review) is the author/funder, who has granted bioRxiv a license to display the preprint in perpetuity. It is made available under aCC-BY-NC-ND 4.0 International license.

Ground-truth generation. Realistic deformation was achieved by generating displacements fields that satisfy the theoretical properties of distortion. The displacements along the PE axis of the dMRI image are related to the local deviation of the field $\Delta B_0(\mathbf{r})$ from its nominal value B_0 (Jezzard and Balaban, 1995), as follows:

$$u_{\text{PE}} = \frac{\gamma\, T_{acq}\, s_{\text{PE}}}{2\pi} \Delta B_0(\mathbf{r}) \text{ [mm]}, \tag{13}$$

where γ is the gyromagnetic ratio, T_{acq} is the readout time, and s_{PE} is the pixel size along PE. Certain MR sequences are designed to estimate ΔB_0, thereby obtaining the so-called fieldmap. We derived the deformation U_{true} from the fieldmap image released with the corresponding packages of each dataset in the HCP. The fieldmap was unwrapped[2] and smoothed before applying (13). Next, the original dMRI was warped using the resulting displacement field and fed into a pipeline to process the corresponding DTI, thereby computing the derived scalars of interest (FA and ADC) using *MRtrix* (Tournier et al., 2012).

Metric assessment. Initially, we investigated the appropriateness of the segmentation model. For five test datasets, we uniformly sampled the space of distortions $\hat{U} = \epsilon \cdot U_{\text{true}} = \mathbf{r} + \epsilon\, u_{\text{PE}}$ (with $\epsilon \in [-1.1, 1.1]$ and u_{PE} from (13)), and we evaluated the data term of the cost function (7). The minimum of the cost function (subsection 2.1) was consistently located at $\epsilon = 0.0$ (the ground-truth) for all of the cases (Supplemental Materials, figure S2).

Settings. *Regseg* accepts an affine mapping from surface-space to the dMRI data as initialization. However, the images provided by the HCP are already spatially normalized. Therefore, the initial estimation of distortion is zero in this experiment. Since the distortion U_{true} is aligned along the PE direction (y-axis in our settings), *regseg* was configured to allow nonzero displacements only on that corresponding direction. For the experiments on real data, *regseg* established a multi-resolution pyramid of B-Spline functions, with control points distributed on grids of the following spacings: 40×100×40 [mm] for the first (coarser) level, 30×30×30 [mm] for the second level, and 20×30×10 [mm] in the third level. Only the first and second levels included Gaussian smoothing of the target image (σ = [2.0, 0.5] mm, respectively). The actual choices of the parameter settings are publicly distributed with the source code for the experiments[3]. These settings were obtained manually, driven by the feedback obtained from the post-registration convergence reports (like that found in Supplemental Materials, section S1.3). We released *regseg* along with the tool to generate such convergence reports.

Cross-comparison. A dual workflow to the general evaluation used for *regseg* (Figure 4), was employed to integrate the alternate T2B registration scheme. We reproduced the solution and settings provided with *ExploreDTI* (Leemans et al., 2009), which is a widely used toolkit for tractography analysis of DTI. *ExploreDTI* internally employs *elastix* (Klein et al., 2010) to perform registration. The deformation field is correspondingly restricted to the PE direction. The settings file for *elastix* is also available[4].

Error measurement. Distortion only occurs along the PE axis of the image, so we computed the surface warping index (sWI) as the area-weighted distance between the corresponding vertices of $\mathbf{\Gamma}_{\text{true}}$ and their estimate obtained by the method under the test $\hat{\mathbf{\Gamma}}_{\text{test}}$:

$$sWI = \frac{1}{\sum_i a_i} \sum_i^{N_V} a_i \, \|\mathbf{v}_i - \hat{\mathbf{v}}_i\|, \tag{14}$$

where $\mathbf{v}_i \subset \mathbf{\Gamma}_{\text{true}}$ are the locations of the total N_V vertices and $\hat{\mathbf{v}}_i \subset \hat{\mathbf{\Gamma}}_{\text{test}}$ are the recovered locations that correspond to $\mathbf{v}_i$. In practice, we only report the sWI for three surfaces ($\{\Gamma_{VdGM}, \Gamma_{WM}, \Gamma_{pial}\}$) of crucial interest in whole-brain tractography.

[2] fieldmaps are phase maps, which are intrinsically clipped in the interval of $[-\pi, \pi)$ [rads] or [rads/s].
[3] https://github.com/oesteban/RegSeg/tree/master/Scripts/pyacwereg/data/regseg_hcp.json
[4] https://github.com/oesteban/RegSeg/blob/master/Scripts/pyacwereg/data/t2b_elastix_y.txt

bioRxiv preprint doi: https://doi.org/10.1101/018945; this version posted November 11, 2015. The copyright holder for this preprint (which was not certified by peer review) is the author/funder, who has granted bioRxiv a license to display the preprint in perpetuity. It is made available under aCC-BY-NC-ND 4.0 International license.

3. Results

3.1. Verification and validation using digital phantoms

The results summarized in Figure 5 demonstrated that the accuracy was high and below the image resolution. Panel B on Figure 5 shows the violin plots for each model type corresponding to the two sets of resolutions for the generated phantoms. In order to relate the average misregistration error to the resolution of the moving image, we proceeded as follows. First, we confirmed that the vertex-wise error distributions were skewed by using Shapiro-Wilk's test of normality. All of the distributions of errors in the tests (four phantom types $\times$ two resolutions) were nonnormal with $p < 0.001$. Consequently, we used the nonparametric Wilcoxon signed-rank test with the Bonferroni correction for multiple comparisons (N=150, for each phantom type). The average errors were significantly lower than the voxel size with $p <$ (0.001 / 150) in all tests (four phantom types $\times$ two resolutions). Statistical tests might not be sufficiently conclusive, so we also computed the confidence intervals, as shown in Table 1.

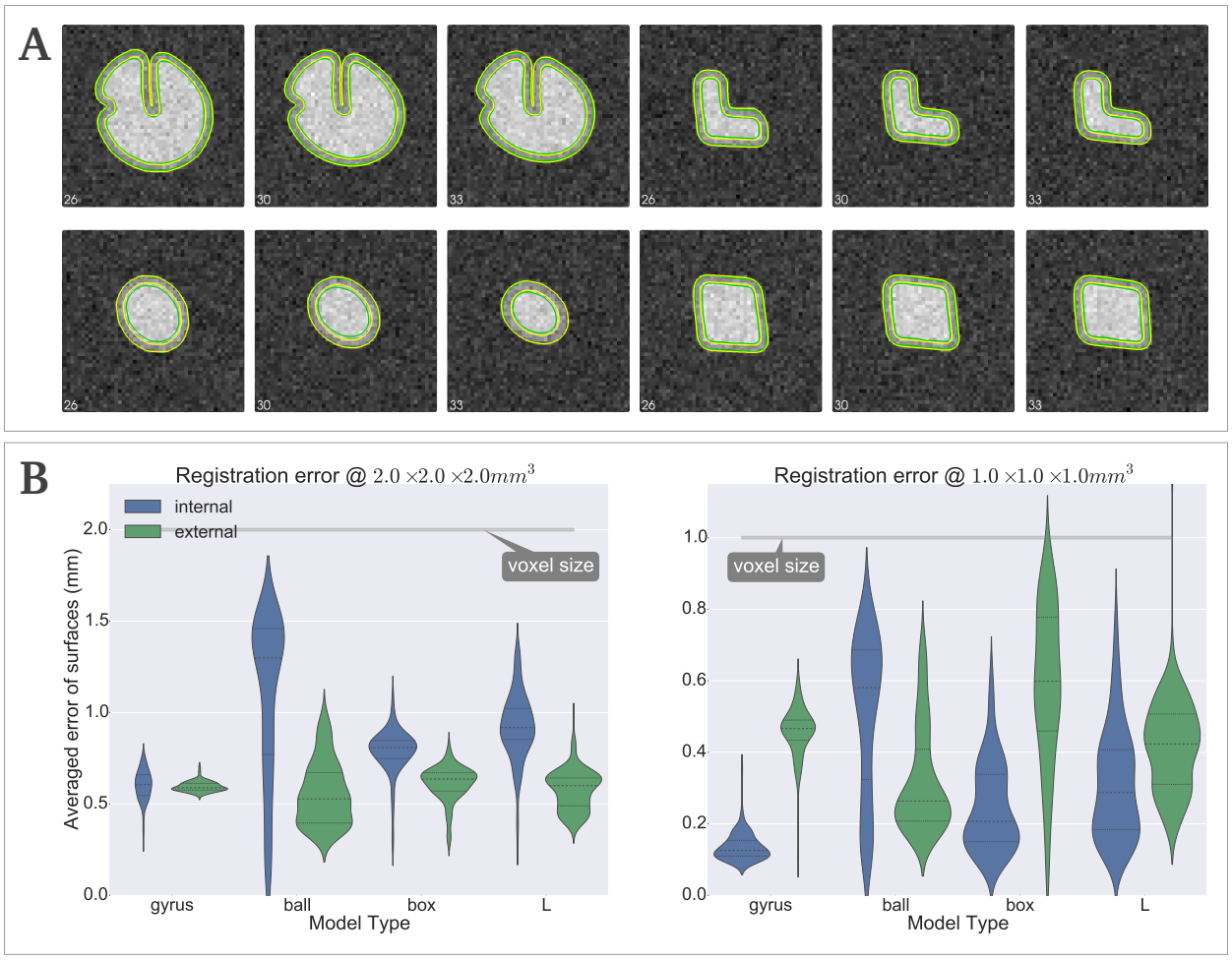

Figure 5: A. Visual assessment of the results obtained with the low resolution sets: "gyrus" (top left), "L" (top right), "ball" (bottom left), and "box" at (bottom right). The contours recovered after registration are represented in yellow. *Regseg* achieved high accuracy because it determined the almost exact locations of the registered contours with respect to their ground truth positions (shown in green). The partial volume effect makes segmentation of the sulci a challenging problem with voxel-wise clustering methods, but they were successfully segmented with *regseg*. B. Quantitative evaluation of registration errors in terms of the average Hausdorff distances between surfaces at low (left) and high (right) resolutions, which demonstrate that the errors were consistently below the size of the voxels.

bioRxiv preprint doi: https://doi.org/10.1101/018945; this version posted November 11, 2015. The copyright holder for this preprint (which was not certified by peer review) is the author/funder, who has granted bioRxiv a license to display the preprint in perpetuity. It is made available under aCC-BY-NC-ND 4.0 International license.

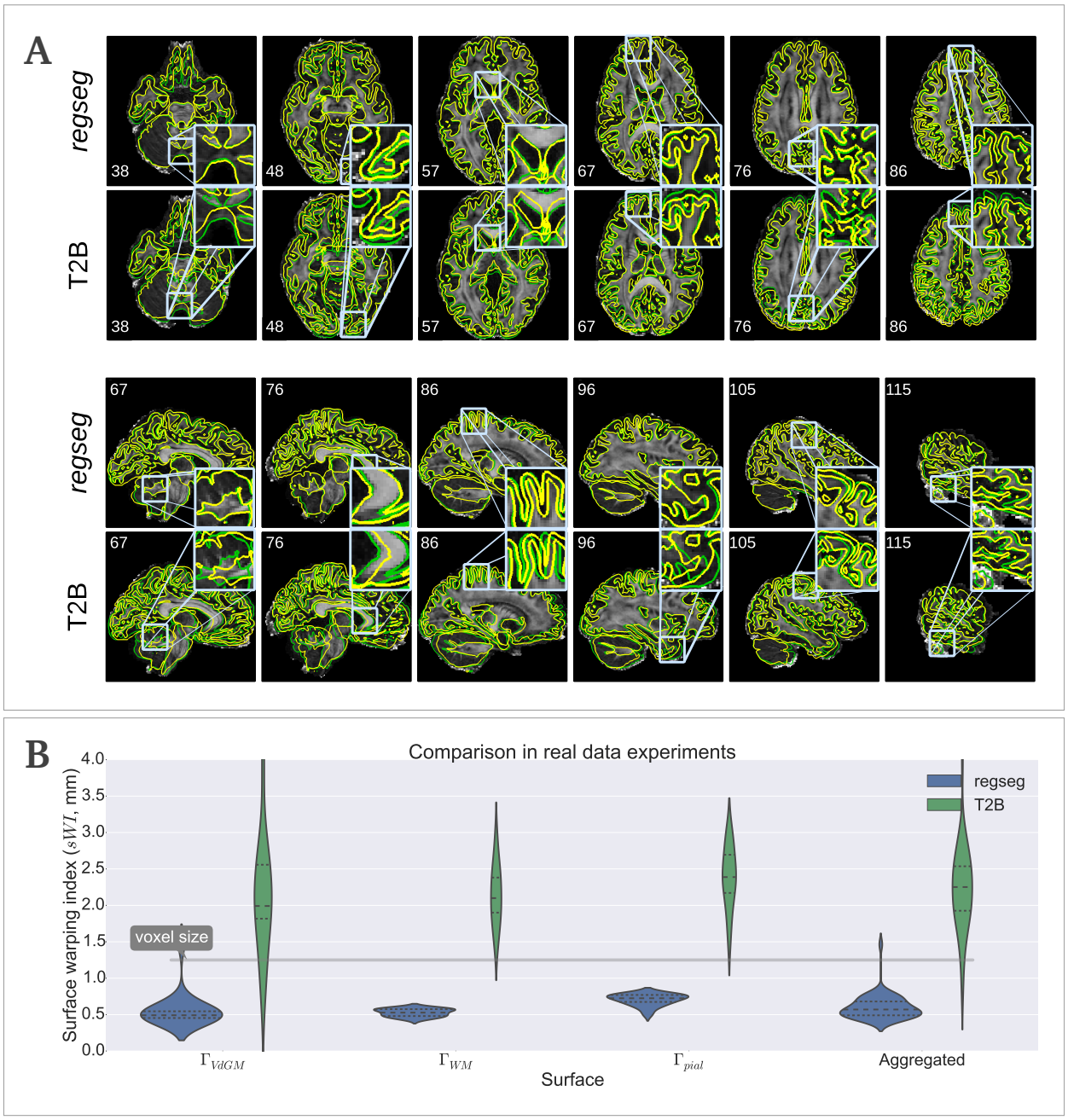

Figure 6: A. Example of a visual assessment report, which was automatically generated by the evaluation tool. Each view shows one component of the input image (in this case, the FA map), the ground-truth locations of the surfaces (green contours), and the resulting surfaces obtained with the test method (yellow contours). The first two rows show axial slices for *regseg* and the T2w-registration based (T2B) method, while the last two rows show the corresponding sagittal views. The coronal view is omitted because it was the least informative due to the directional property of the distortions. Specific regions where *regseg* outperformed T2B are enlarged. B. Violin plots of the error distributions for each surface, which show the voxel size of the dMRI images (1.25 mm), thereby supporting the improved results obtained by *regseg* with the proposed settings.

bioRxiv preprint doi: https://doi.org/10.1101/018945; this version posted November 11, 2015. The copyright holder for this preprint (which was not certified by peer review) is the author/funder, who has granted bioRxiv a license to display the preprint in perpetuity. It is made available under aCC-BY-NC-ND 4.0 International license.

Res.	"gyrus"	"ball"	"box"	"L"	Aggreg.
1.0mm	0.18–0.38	0.31–0.45	0.34–0.42	0.34–0.40	0.34–0.38
2.0mm	0.59–0.60	0.65–0.76	0.68–0.71	0.67–0.77	0.64–0.66

Table 1: The distributions of vertex-wise Hausdorff distances between the ground-truth surfaces and their corresponding estimates obtained with *regseg* presented a 95% CI below the half-voxel size for all of the phantom types. The CIs were computed by bootstrapping using 10^4 samples, with the median as the location statistic.

		Γ_{VdGM}	Γ_{WM}	Γ_{pial}	Aggreg.
CI	*regseg*	0.50–0.78	0.50–0.55	0.66–0.73	0.56–0.66
	T2B	1.78–2.58	1.94–2.36	2.16–2.58	2.05–2.39
H-tests	p-value	$4.1{\cdot}10^{-6}$	$2.3{\cdot}10^{-6}$	$2.3{\cdot}10^{-6}$	$1.8{\cdot}10^{-16}$
	H-stat	21.20	22.31	22.31	67.85

Table 2: Statistical analysis of results obtained using real data, which show that *regseg* performed better than the alternative T2w-registration based (T2B) method. The distribution of the errors computed for the surfaces of interest (Γ_{VdGM}, Γ_{WM}, Γ_{pial}) and the aggregate of all surfaces (Aggreg. column) had lower 95% CIs with *regseg*. The CIs in this table were computed by bootstrapping using the mean as the location statistic and with 10^4 samples. The Kruskal-Wallis H-tests indicated that there was a significant difference between the results obtained using *regseg* and the T2B method.

3.2. Evaluation using real datasets and cross-comparison

Finally, we compared the performance of *regseg* with that of the standard T2B method. Summary reports for visual assessment of the 16 cases are included in the Supplemental Materials, section S5. In Figure 6, box A, the visual report is shown for one subject. We computed the sWI (14) of every surface after registration using both the *regseg* and T2B methods. Finally, to compare the results, we performed Kruskal-Wallis H-tests (a nonparametric alternative to ANOVA) on the warping indices for the three surfaces of interest selected in section 2.5 (Γ_{VdGM}, Γ_{WM}, Γ_{pial}). All of the statistical tests showed that the error distributions obtained with *regseg* and T2B were significantly different, and the violin plots in box B of Figure 6 demonstrate that the errors were always larger with T2B. We also show the 95% CIs of the sWI for these surfaces. The aggregate CI for *regseg* was 0.56–0.66 [mm], whereas the T2B method yielded an aggregate CI of 2.05–2.39 [mm]. The results of the statistical tests and the CIs are summarized in Table 2.

4. Discussion

We present *regseg*, a simultaneous segmentation and registration method that maps a set of nested surfaces into a multivariate target-image. The nonlinear registration process evolves driven by the fitness of the picewise-smooth classification of voxels in the target volume imposed by the current mapping of the surfaces. We propose *regseg* to map anatomical information extracted from T1w images into the corresponding dMRI of the same subject. Previously, joint segmentation and registration has been applied successfully to other problems such as longitudinal object tracking (Paragios, 2003) and atlas-based segmentation (Gorthi et al., 2011). The most common approach involves optimizing a deformation model (registration) that supports the evolution of the active contours (segmentation), like Paragios (2003); Yezzi et al. (2003). *Regseg* can be seen as a particular case of atlas-based segmentation-registration methods, replacing the atlas by the structural image of the subject (*structure-informed segmentation*). The main difference of atlas-based segmentation and the application at hand is the resolution of the target image. Atlas-based segmentation is typically applied on structural and high-resolution images. A comprehensive review of joint segmentation and registration methods applied in atlas-based segmentation is found in (Gorthi et al., 2011). They also propose a multiphase level-set function initialized from a labeled atlas to implement the active contours that drive the atlas registration. Alternatively, *regseg* implements the active contours with a hierarchical set of explicit surfaces (triangular meshes) instead of the multiphase level sets, and registration is driven by shape-gradients (Herbulot et al., 2006). As an advantage, the use of explicit surfaces enables segmenting dMRI images with accuracy below pixel size.

An important antecedent of *regseg* is *bbregister* (Greve and Fischl, 2009). The tool has been widely adopted as the standard registration method to be used along with the EPI correction of choice. It implements a linear mapping and uses 3D active contours *with edges* to search for intensity boundaries in the *b0* image. The active contours are initialized using surfaces extracted from the T1w using *FreeSurfer* (Fischl, 2012). To overcome the problem of nonlinear distortions, *bbregister* excludes from the boundary search

bioRxiv preprint doi: https://doi.org/10.1101/018945; this version posted November 11, 2015. The copyright holder for this preprint (which was not certified by peer review) is the author/funder, who has granted bioRxiv a license to display the preprint in perpetuity. It is made available under aCC-BY-NC-ND 4.0 International license.

those regions that are typically warped. Indeed, the distortion must be addressed separately because it is not supported by the affine transformation model. Conversely, the deformation model of *regseg* is nonlinear and the active contours are *without edges* (Chan and Vese, 2001) since the FA and ADC maps do not present steep image gradients (edges) but the anatomy can be identified by looking for piece-wise smooth homogeneous regions.

Recently, Le Guyader and Vese (2011) proposed a simultaneous segmentation and registration method in 2D using level sets and a nonlinear elasticity smoother on the displacement vector field, which preserves the topology even with very large deformations. *Regseg* includes an anisotropic regularizer for the displacements field proposed by Nagel and Enkelmann (1986). This regularization strategy conceptually falls in the midway between the Gaussian smoothing generally included in most of the existing methodologies, and the complexity of the elasticity smoother of Le Guyader and Vese (2011). Other minor features that differ from current methods in joint segmentation and registration are the support of multivariate target-images and the efficient computation of the shape-gradients implemented with sparse matrices.

We verified that precise segmentation and registration of a set of surfaces into multivariate data is possible on digital phantoms. We randomly deformed four different phantom models to mimic three homogeneous regions (WM, GM, and cerebrospinal fluid) and we used them to simulate T1w and T2w images at two resolution levels. We measured the Hausdorff distance between the contours projected using the ground-truth warping and the estimations found with *regseg*. We concluded that the errors were significantly lower than the voxel size. We also assessed the 95% confidence interval (CI), which yielded an aggregate interval of 0.64–0.66 [mm] for the low resolution phantoms (2.0 mm isotropic voxel) and 0.34–0.38 [mm] for the high resolution phantoms (1.0 mm isotropic). Therefore, the error was bounded above by half of the voxel size. The distributions of errors along surfaces varied importantly depending on the shape of the phantom (see Figure 5B). The misregistration error of the "gyrus" phantom showed a much lower spread than that for the other shapes. We argue that the symmetry of those other shapes posed difficulties in driving the contours towards the appropriate region due to *sliding* displacements between the surfaces and their ground-truth position. The effect is not detectable by the active contours framework, but it is controllable increasing the regularization constraints. When *regseg* is applied on real datasets, this surface sliding is negligible for the convoluted nature of cortical surfaces and the directional restriction of the distortion.

We evaluated *regseg* in a real environment using the experimental framework presented in Figure 4. We processed 16 subjects from the HCP database using both *regseg* and an in-house replication of the T2w-registration based (T2B) method. *Regseg* obtained a high accuracy, with an aggregate 95% CI of 0.56–0.66 [mm], which was below the pixel size of 1.25 mm. The misregistration error that remained after *regseg* was significantly lower ($p < 0.01$) than the error corresponding to the T2B correction according to Kruskal-Wallis H-tests (Table 2). Visual inspections of all the results (Supplemental Materials, section S5) and the violin plots in Figure 6 confirmed that *regseg* achieved higher accuracy than the T2B method in our settings. We carefully configured the T2B method using the same algorithm and the same settings employed in a widely-used tool for dMRI processing. However, cross-comparison experiments are prone to the so-called *instrumentation bias* (Tustison et al., 2013). Therefore, these results did not prove that *regseg is better than* T2B, but indicated that *regseg* is a reliable option in this application field. Finally, we also proposed a piecewise-smooth segmentation model defined by a selection of nested surfaces to partition the multispectral space comprehending the FA and the ADC maps and ultimately identify anatomical structures in dMRI space. We also demonstrated the smoothness of the objective function on five of the real datasets (Supplemental Materials, figure S2), taking advantage of the directional restriction of possible distortions. However, *regseg* requires densely sampled surfaces to ensure the convergence. Using the digital phantoms, we severely decimated the surfaces by a large factor. These surfaces introduced a bias which displaced the zero of the gradients from the minimum of the objective function impeding the convergence.

The proposed application of the method in the task of identifying structural information in dMRI images is an active field of research (Jeurissen et al., 2015). Current processing steps involved in the connectome extraction require a precise segmentation of anatomical structures in the diffusion space. Some examples of these processing tasks are the structure-informed reconstruction of dMRI data (Jeurissen et al., 2014; Daducci et al., 2015), the anatomically constrained tractography (Smith et al., 2012), and the imposition of the cortical parcellation mapped from the T1w image (Hagmann et al., 2008). The problem was firstly

bioRxiv preprint doi: https://doi.org/10.1101/018945; this version posted November 11, 2015. The copyright holder for this preprint (which was not certified by peer review) is the author/funder, who has granted bioRxiv a license to display the preprint in perpetuity. It is made available under aCC-BY-NC-ND 4.0 International license.

addressed using image segmentation approaches in the native diffusion space, without definite and compelling results. With the introduction of retrospective correction methods for the *EPI distortions* and image registration approaches, the task has been typically solved in a two-step approach. First, the DWIs are corrected for *EPI distortions* by estimating the nonlinear deformation field from extra MR acquisitions (Jezzard and Balaban, 1995; Chiou and Nalcioglu, 2000; Cordes et al., 2000; Kybic et al., 2000). Second, mapping the structural information from the corresponding T1w image using a linear registration tool like *bbregister* (Greve and Fischl, 2009). The current activity on improving correction methods (Irfanoglu et al., 2015) and the comeback of segmentation of dMRI in its native space (Jeurissen et al., 2015) proof the open interest of this application. *Regseg* addresses this joint problem in a single step and it does not require any additional acquisition other than the minimal protocol comprehending only T1w and dMRI images. This situation is found commonly in historical datasets. Moreover, since the structural information is projected into the native space of dMRI, the whole connectome extraction process can be performed on the unaltered dMRI signal (i.e. without resampling data to an undistorted space).

Beyond the presented application on dMRI data, *regseg* can be indicated in situations where there are precise surfaces delineating the structure, a target multivariate image in which the surfaces must be fitted, and the mapping between the surfaces and the volume encodes relevant physiological information, such as the normal/abnormal development or the macroscopic dynamics of organs and tissues. For instance, *regseg* may be applied in fields like neonatal brain image segmentation in longitudinal MRI studies of the early developmental patterns (Shi et al., 2010). In these studies, the surfaces obtained in a mature timepoint of the brain are retrospectively propagated to the initial timepoints, regardless of the changes in the contrast and spatial development between them. More generally, *regseg* may also be applied to the personalized study of longitudinal alteration of the brain using multispectral images, for instance in the case of traumatic brain injury (Irimia et al., 2014) or in the monitorization of brain tumors (Weizman et al., 2014).

Conclusion

Regseg is a variational framework for the simultaneous segmentation and registration of 3D dMRI data obtained from the human brain, where within-subject anatomical information is used as a reference. The registration method segments the target multivariate image into several competing regions, which are defined explicitly by their limiting surfaces. The surfaces are active and they evolve on a free-form deformation field supported by the B-spline basis. A descent optimization strategy is guided by shape gradients computed on the current partition of the target image. *Regseg* uses active contours without edges and it searches for homogeneous regions within the image. We tested *regseg* using digital phantoms by simulating T1w and T2w magnetic resonance imaging (MRI) warped with smooth random deformations. The resulting misregistration of the contours was significantly lower than the image resolution of the phantoms.

We proposed *regseg* for simultaneously segmenting and registering dMRI data to their corresponding T1w image from the same subject. We demonstrated the accuracy of the proposed method based on visual assessments of the results obtained by *regseg* and cross-comparisons with a widely used technique. Moreover, *regseg* does not require any images in addition to the minimal acquisition protocol, which only utilizes T1w and dMRI. As well as the proposed application to dMRI data, other potential uses of *regseg* are atlas-based segmentation and tracking objects in time-series.

Availability and reproducibility statement

We considered the reproducibility of our results as a design requirement. Therefore, we used real data obtained from the Human Connectome Project (Van Essen et al., 2012) and all of the software utilized in this study is also publicly available. *Regseg* was implemented on top of ITK-4.6 (Insight Registration and Segmentation Toolkit, `http://www.itk.org`). The evaluation instruments (Figure 4) were implemented using *nipype* (Gorgolewski et al., 2011) to assess their reproducibility. All of the research elements (data, source code, figures, manuscript sources, etc.) involved in this study are publicly available under a unique package (Esteban and Zosso, 2015).

bioRxiv preprint doi: https://doi.org/10.1101/018945; this version posted November 11, 2015. The copyright holder for this preprint (which was not certified by peer review) is the author/funder, who has granted bioRxiv a license to display the preprint in perpetuity. It is made available under aCC-BY-NC-ND 4.0 International license.

Author contributions

All the authors contributed to this study. OE implemented the method, designed and conducted the experiments, wrote the paper, simulated the phantoms, and prepared the real data. DZ devised and drafted the registration method, generated early phantom datasets, and collaborated in the implementation of the method. AD, MBC, and MJLC interpreted the results. AD, MBC, MJLC, JPT, and AS advised on all aspects of the study.

Acknowledgments

The authors thank Y. Alemán and G. Wollny for their thorough reviews of the manuscript, V. Estellers for early discussions at the beginning of this project, and L. A. Vese for her support during OE's research visits to her laboratory. We also thank A. Leemans for kindly sharing a p-code version of *ExploreDTI* from which the settings for *elastix* could be extracted.

DZ was supported by the Swiss National Science Foundation under grants PBELP2-137727, P300P2-147778, and NSF-DMS 1418812. This study was supported by the Spanish Ministry of Science and Innovation (projects TEC-2013-48251-C2-2-R and INNPACTO XIORT), Comunidad de Madrid (TOPUS) and European Regional Development Funds, the Center for Biomedical Imaging (CIBM) of the Geneva and Lausanne Universities and the EPFL, as well as the Leenaards and Louis Jeantet Foundations.

Appendix

Appendix 1. Simplifying the regularization term

The exponentials of the Thikonov regularization prior (6) have the general form $\mathbf{v}^T\mathbf{M}\mathbf{v}$. If $\mathbf{M}$ is a $n \times n$ diagonal matrix such that $\mathbf{M} = \mathbf{m}\,\mathbf{I}_n$, then:

$$\mathbf{v}^T\mathbf{M}\mathbf{v} = \mathbf{m} \cdot (\mathbf{v}^T\mathbf{I}_n\mathbf{v}) = \mathbf{m} \cdot \mathbf{v}^{\circ 2},$$

where we have introduced the Hadamard power notation[5].

In general, the anisotropy is aligned with the imaging axes, so $\mathbf{A}$ and $\mathbf{B}$ of (7) can be simplified to diagonal matrices, such that $\mathbf{A} = \boldsymbol{\alpha}\,\mathbf{I}_n$ and $\mathbf{B} = \boldsymbol{\beta}\,\mathbf{I}_n$. By substituting into equation (7), we obtain:

$$E(\mathbf{u}) = \text{Const.} + \sum_l \int_{\Omega_l} \mathcal{D}_l^2(\mathbf{f}')\, d\mathbf{r} + \\ + \int_\Omega \frac{1}{2}\left[\boldsymbol{\alpha} \cdot \mathbf{u}^{\circ 2} + \boldsymbol{\beta} \cdot (\nabla \mathbf{u})^{\circ 2}\right] d\mathbf{r}. \tag{A.1}$$

References

J. L. R. Andersson, J. Xu, E. Yacoub, E. Auerbach, S. Moeller, and K. Ugurbil. A comprehensive gaussian process framework for correcting distortions and movements in diffusion images. In *20th ISMRM*, p. 2426, Melbourne, Australia, 2012.

P. Basser and C. Pierpaoli. Microstructural and physiological features of tissues elucidated by quantitative-diffusion-tensor MRI. *J Magn Reson B*, 111(3):209–219, 1996. doi:10.1016/j.jmr.2011.09.022.

E. Caruyer, A. Daducci, M. Descoteaux, J.-C. Houde, J.-P. Thiran, and R. Verma. Phantomas: a flexible software library to simulate diffusion MR phantoms. In *23th ISMRM*, Milano, Italy, 2014.

T. F. Chan and L. A. Vese. Active contours without edges. *IEEE Trans Image Process*, 10(2):266–277, 2001. doi:10.1109/83.902291.

J. Y. Chiou and O. Nalcioglu. A simple method to correct off-resonance related distortion in echo planar imaging. In *8th ISMRM*, p. 1711, Denver, USA, 2000.

[5]The Hadamard power of a matrix or a vector is the power of its elements $\mathbf{M}^{\circ p} = ({m_{ij}}^p)$

bioRxiv preprint doi: https://doi.org/10.1101/018945; this version posted November 11, 2015. The copyright holder for this preprint (which was not certified by peer review) is the author/funder, who has granted bioRxiv a license to display the preprint in perpetuity. It is made available under aCC-BY-NC-ND 4.0 International license.

F. Commandeur, J. Velut, and O. Acosta. A VTK algorithm for the computation of the Hausdorff distance. *VTK Journal*, 839, 2011.

D. Cordes, K. Arfanakis, V. Haughton, and M. Meyerand. Geometric distortion correction in EPI using two images with orthogonal phase-encoding directions. In *8th ISMRM*, p. 1712, Denver, USA, 2000.

R. C. Craddock, S. Jbabdi, C.-G. Yan, J. T. Vogelstein, F. X. Castellanos, A. Di Martino, C. Kelly, K. Heberlein, S. Colcombe, and M. P. Milham. Imaging human connectomes at the macroscale. *Nat Meth*, 10(6):524–539, 2013. doi:10.1038/nmeth.2482.

M. Cuadra, L. Cammoun, T. Butz, O. Cuisenaire, and J. P. Thiran. Comparison and validation of tissue modelization and statistical classification methods in T1 weighted MR brain images. *IEEE Trans Med Imag*, 24(12):1548–1565, 2005. doi:10.1109/TMI.2005.857652.

A. Daducci, E. J. Canales-Rodríguez, H. Zhang, T. B. Dyrby, D. C. Alexander, and J.-P. Thiran. Accelerated Microstructure Imaging via Convex Optimization (AMICO) from diffusion MRI data. *NeuroImage*, 105:32–44, 2015. doi:10.1016/j.neuroimage.2014.10.026.

D. B. Ennis and G. Kindlmann. Orthogonal tensor invariants and the analysis of diffusion tensor magnetic resonance images. *Magn Reson Med*, 55(1):136–146, 2006. doi:10.1002/mrm.20741.

O. Esteban and D. Zosso. RegSeg: Structure-informed segmentation and registration of brain MR images. *Zenodo [Software]*, 2015. doi:10.5281/zenodo.33282.

O. Esteban, A. Daducci, E. Caruyer, K. O'Brien, M. J. Ledesma-Carbayo, M. Bach-Cuadra, and A. Santos. Simulation-based evaluation of susceptibility distortion correction methods in diffusion MRI for connectivity analysis. In *11th ISBI*, pp. 738–741, Beijing, China, 2014. doi:10.1109/ISBI.2014.6867976.

O. Esteban, G. Wollny, S. Gorthi, M.-J. Ledesma-Carbayo, J.-P. Thiran, A. Santos, and M. Bach-Cuadra. MBIS: Multivariate Bayesian Image Segmentation tool. *Comp Meth Prog Biomed*, 115(2):76–94, 2014. doi:10.1016/j.cmpb.2014.03.003.

O. Esteban, D. Zosso, A. Daducci, M. Bach-Cuadra, M. J. Ledesma-Carbayo, J.-P. Thiran, and A. Santos. Useful data and software instruments in verification and validation of segmentation and registration methods for diffusion MRI (Supplemental Materials). *Data Brief*, (submitted), 2015. doi:10.6084/m9.figshare.1397502.

B. Fischl. FreeSurfer. *NeuroImage*, 62(2):774–781, 2012. doi:10.1016/j.neuroimage.2012.01.021.

T. Gass, G. Székely, and O. Goksel. Simultaneous segmentation and multiresolution nonrigid atlas registration. *IEEE Trans Image Process*, 23(7):2931–2943, 2014. doi:10.1109/TIP.2014.2322447.

M. F. Glasser, S. N. Sotiropoulos, J. A. Wilson, T. S. Coalson, B. Fischl, J. L. Andersson, J. Xu, S. Jbabdi, M. Webster, J. R. Polimeni, D. C. Van Essen, and M. Jenkinson. The minimal preprocessing pipelines for the Human Connectome Project. *NeuroImage*, 80:105–124, 2013. doi:10.1016/j.neuroimage.2013.04.127.

K. Gorgolewski, C. D. Burns, C. Madison, D. Clark, Y. O. Halchenko, M. L. Waskom, and S. Ghosh. Nipype: a flexible, lightweight and extensible neuroimaging data processing framework in Python. *Front Neuroinform*, 5:13, 2011. doi:10.3389/fninf.2011.00013.

S. Gorthi, V. Duay, X. Bresson, M. Bach Cuadra, F. J. Sánchez Castro, C. Pollo, A. S. Allal, and J.-P. Thiran. Active deformation fields: dense deformation field estimation for atlas-based segmentation using the active contour framework. *Med Image Anal*, 15(6): 787–800, 2011. doi:10.1016/j.media.2011.05.008.

D. N. Greve and B. Fischl. Accurate and robust brain image alignment using boundary-based registration. *NeuroImage*, 48(1):63–72, 2009. doi:10.1016/j.neuroimage.2009.06.060.

A. Hadjiprocopis, W. Rashid, and P. S. Tofts. Unbiased segmentation of diffusion-weighted magnetic resonance images of the brain using iterative clustering. *Magn Res Imag*, 23(8):877–885, 2005. doi:10.1016/j.mri.2005.07.010.

P. Hagmann, L. Cammoun, X. Gigandet, R. Meuli, C. J. Honey, V. J. Wedeen, and O. Sporns. Mapping the structural core of human cerebral cortex. *PLoS Biol*, 6(7):e159, 2008. doi:10.1371/journal.pbio.0060159.

D. Han, V. Singh, J. Lee, E. Zakszewski, N. Adluru, T. Oakes, and A. Alexander. An experimental evaluation of diffusion tensor image segmentation using graph-cuts. In *31th EMBC*, pp. 5653–5656, Minneapolis, Minnesota, USA, 2009. doi:10.1109/IEMBS.2009.5333767.

A. Herbulot, S. Jehan-Besson, S. Duffner, M. Barlaud, and G. Aubert. Segmentation of Vectorial Image Features Using Shape Gradients and Information Measures. *J Math Imaging Vis*, 25(3):365–386, 2006. doi:10.1007/s10851-006-6898-y.

D. Holland, J. M. Kuperman, and A. M. Dale. Efficient Correction of Inhomogeneous Static Magnetic Field-Induced Distortion in Echo Planar Imaging. *NeuroImage*, 50(1):175–183, 2010. doi:10.1016/j.neuroimage.2009.11.044.

M. O. Irfanoglu, L. Walker, S. Sammet, C. Pierpaoli, and R. Machiraju. Susceptibility Distortion Correction for Echo Planar Images with Non-uniform B-Spline Grid Sampling: A Diffusion Tensor Image Study. In *14th MICCAI*, LNCS 6892, pp. 174–181, Toronto, Canada, 2011. Springer Berlin Heidelberg. doi:10.1007/978-3-642-23629-7_22.

M. O. Irfanoglu, P. Modi, A. Nayak, E. B. Hutchinson, J. Sarlls, and C. Pierpaoli. DR-BUDDI (Diffeomorphic Registration for Blip-Up blip-Down Diffusion Imaging) method for correcting echo planar imaging distortions. *NeuroImage*, 106:284–299, 2015. doi:10.1016/j.neuroimage.2014.11.042.

A. Irimia, S.-Y. M. Goh, C. M. Torgerson, P. M. Vespa, and J. D. Van Horn. Structural and connectomic neuroimaging for the personalized study of longitudinal alterations in cortical shape, thickness and connectivity after traumatic brain injury. *J Neurosurg Sci*, 58(3): 129–144, 2014.

S. Jehan-Besson, M. Barlaud, and G. Aubert. DREAM2S: Deformable Regions Driven by an Eulerian Accurate Minimization Method for Image and Video Segmentation. *Int J Comput Vis*, 53(1):45–70, 2003. doi:10.1023/A:1023031708305.

B. Jeurissen, J.-D. Tournier, T. Dhollander, A. Connelly, and J. Sijbers. Multi-tissue constrained spherical deconvolution for improved analysis of multi-shell diffusion MRI data. *NeuroImage*, 103:411–426, 2014. doi:10.1016/j.neuroimage.2014.07.061.

B. Jeurissen, J.-D. Tournier, and J. Sijbers. Tissue-type segmentation using non-negative matrix factorization of multi-shell diffusion-weighted MRI images. In *23th ISMRM*, p. 0346, Toronto, Canada, 2015.

P. Jezzard and R. S. Balaban. Correction for geometric distortion in echo planar images from B0 field variations. *Magn Reson Med*, 34 (1):65–73, 1995. doi:10.1002/mrm.1910340111.

L. Jonasson. *Segmentation of diffusion weighted MRI using the level set framework*. Ph.D. Thesis, École Polytechnique Fédérale de Lausanne, Lausanne (Swizerland), 2005.

S. Klein, M. Staring, K. Murphy, M. Viergever, and J. P. W. Pluim. elastix: A Toolbox for Intensity-Based Medical Image Registration.

bioRxiv preprint doi: https://doi.org/10.1101/018945; this version posted November 11, 2015. The copyright holder for this preprint (which was not certified by peer review) is the author/funder, who has granted bioRxiv a license to display the preprint in perpetuity. It is made available under aCC-BY-NC-ND 4.0 International license.

IEEE Trans Med Imag, 29(1):196–205, 2010. doi:10.1109/TMI.2009.2035616.

J. Kybic, P. Thevenaz, A. Nirkko, and M. Unser. Unwarping of unidirectionally distorted EPI images. *IEEE Trans Med Imag*, 19(2):80–93, 2000. doi:10.1109/42.836368.

C. Le Guyader and L. A. Vese. A combined segmentation and registration framework with a nonlinear elasticity smoother. *Comput Vis Image Und*, 115(12):1689–1709, 2011. doi:10.1016/j.cviu.2011.05.009.

A. Leemans, B. Jeurissen, J. Sijbers, and D. Jones. ExploreDTI: a graphical toolbox for processing, analyzing, and visualizing diffusion MR data. In *17th ISMRM*, p. 3537, Hawaii, USA, 2009.

T. Liu, H. Li, K. Wong, A. Tarokh, L. Guo, and S. T. Wong. Brain tissue segmentation based on DTI data. *NeuroImage*, 38(1):114–123, 2007. doi:10.1016/j.neuroimage.2007.07.002.

C.-F. Lu, P.-S. Wang, Y.-C. Chou, H.-C. Li, B.-W. Soong, and Y.-T. Wu. Segmentation of diffusion-weighted brain images using expectation maximization algorithm initialized by hierarchical clustering. In *30th EMBS*, pp. 5502–5505, Vancouver, Canada, 2008. doi:10.1109/IEMBS.2008.4650460.

S. Mori, B. J. Crain, V. P. Chacko, and P. C. M. Van Zijl. Three-dimensional tracking of axonal projections in the brain by magnetic resonance imaging. *Ann Neurol*, 45(2):265–269, 1999. doi:10.1002/1531-8249(199902)45:2 extless265::AID-ANA21 extgreater3.0.CO;2-3.

H.-H. Nagel and W. Enkelmann. An Investigation of Smoothness Constraints for the Estimation of Displacement Vector Fields from Image Sequences. *IEEE Trans Pattern Anal Mach Intell*, 8(5):565–593, 1986. doi:10.1109/TPAMI.1986.4767833.

N. Paragios. A level set approach for shape-driven segmentation and tracking of the left ventricle. *IEEE Trans Med Imag*, 22(6):773–776, 2003. doi:10.1109/TMI.2003.814785.

K. M. Pohl, J. Fisher, W. E. L. Grimson, R. Kikinis, and W. M. Wells. A Bayesian model for joint segmentation and registration. *NeuroImage*, 31(1):228–39, 2006. doi:10.1016/j.neuroimage.2005.11.044.

M. Rousson, C. Lenglet, and R. Deriche. Level Set and Region Based Surface Propagation for Diffusion Tensor MRI Segmentation. In *8th ECCV*, LNCS 3117, pp. 123–134, Prague, Czech Republic, 2004. Springer Berlin Heidelberg. doi:10.1007/978-3-540-27816-0_11.

D. Rueckert, P. Aljabar, R. A. Heckemann, J. V. Hajnal, and A. Hammers. Diffeomorphic Registration Using B-Splines. In *9th MICCAI*, LNCS 4191, pp. 702–709, Copenhagen, Denmark, 2006. Springer Berlin Heidelberg. doi:10.1007/11866763_86.

F. Shi, Y. Fan, S. Tang, J. H. Gilmore, W. Lin, and D. Shen. Neonatal Brain Image Segmentation in Longitudinal MRI Studies. *NeuroImage*, 49(1):391–400, 2010. doi:10.1016/j.neuroimage.2009.07.066.

R. E. Smith, J.-D. Tournier, F. Calamante, and A. Connelly. Anatomically-constrained tractography: Improved diffusion MRI streamlines tractography through effective use of anatomical information. *NeuroImage*, 62(3):1924–1938, 2012. doi:10.1016/j.neuroimage.2012.06.005.

C. Studholme, R. Constable, and J. Duncan. Accurate alignment of functional EPI data to anatomical MRI using a physics-based distortion model. *IEEE Trans Med Imag*, 19(11):1115–1127, 2000. doi:10.1109/42.896788.

T. Taoka, M. Morikawa, T. Akashi, T. Miyasaka, H. Nakagawa, K. Kiuchi, T. Kishimoto, and K. Kichikawa. Fractional anisotropy–threshold dependence in tract-based diffusion tensor analysis: evaluation of the uncinate fasciculus in Alzheimer disease. *AJNR Am J Neuroradiol*, 30(9):1700–1703, 2009. doi:10.3174/ajnr.A1698.

J.-D. Tournier, F. Calamante, and A. Connelly. MRtrix: Diffusion tractography in crossing fiber regions. *Int J Imag Syst Tech*, 22(1): 53–66, 2012. doi:10.1002/ima.22005.

N. J. Tustison, H. J. Johnson, T. Rohlfing, A. Klein, S. S. Ghosh, L. Ibanez, and B. B. Avants. Instrumentation bias in the use and evaluation of scientific software: recommendations for reproducible practices in the computational sciences. *Front Neurosci*, 7:162, 2013. doi:10.3389/fnins.2013.00162.

D. Van Essen, K. Ugurbil, E. Auerbach, D. Barch, T. Behrens, R. Bucholz, A. Chang, L. Chen, M. Corbetta, S. Curtiss, S. Della Penna, D. Feinberg, M. Glasser, N. Harel, A. Heath, L. Larson-Prior, D. Marcus, G. Michalareas, S. Moeller, R. Oostenveld, S. Petersen, F. Prior, B. Schlaggar, S. Smith, A. Snyder, J. Xu, and E. Yacoub. The Human Connectome Project: A data acquisition perspective. *NeuroImage*, 62(4):2222–2231, 2012. doi:10.1016/j.neuroimage.2012.02.018.

K. Van Leemput, F. Maes, D. Vandermeulen, and P. Suetens. Automated model-based tissue classification of MR images of the brain. *IEEE Trans Med Imag*, 18(10):897–908, 1999. doi:10.1109/42.811270.

L. Weizman, L. B. Sira, L. Joskowicz, D. L. Rubin, K. W. Yeom, S. Constantini, B. Shofty, and D. B. Bashat. Semiautomatic segmentation and follow-up of multicomponent low-grade tumors in longitudinal brain MRI studies. *Med Phys*, 41(5):052303, 2014. doi:10.1118/1.4871040.

P. P. Wyatt and J. Noble. MAP MRF joint segmentation and registration of medical images. *Med Image Anal*, 7(4):539–552, 2003. doi:10.1016/S1361-8415(03)00067-7.

A. Yezzi, L. Zöllei, and T. Kapur. A variational framework for integrating segmentation and registration through active contours. *Med Image Anal*, 7(2):171–185, 2003. doi:10.1016/S1361-8415(03)00004-5.

L. Zhukov, K. Museth, D. Breen, R. Whitaker, and A. Barr. Level set modeling and segmentation of DT-MRI brain data. *J Electron Imaging*, 12(1):125–133, 2003. doi:10.1117/1.1527628.